



Cite this: *RSC Adv.*, 2020, 10, 5260

# Photocatalytic properties and energy band offset of a tungsten disulfide/graphitic carbon nitride van der Waals heterojunction

Jianjun Liu <sup>\*ab</sup> and Enda Hua<sup>c</sup>

Semiconductor heterojunctions have higher photocatalytic performance than a single photocatalytic material. However, the energy band offset and the photocatalytic reaction mechanism of these heterojunctions remain controversial. Here, tungsten disulfide (WS<sub>2</sub>)/graphitic carbon nitride (GCN) heterojunction photocatalytic water splitting is investigated with the hybrid density functional method. The band structures and the density of states (DOS) indicate that the WS<sub>2</sub>/GCN heterojunction is a type-II heterojunction, and its valence band offset and conduction band offset are 0.27 and 0.04 eV, respectively. The differential charge density distribution and the work function calculation indicate that a built-in electric field is formed in the WS<sub>2</sub>/GCN heterojunction. The potential of the built-in electric field is 0.16 V, and its direction is from the GCN surface to the WS<sub>2</sub> surface. The built-in electric field separates the photogenerated electrons and the holes in space, effectively improving the photocatalytic efficiency of the WS<sub>2</sub>/GCN heterojunction. Our work provides insights into the electronic properties and the photocatalytic hydrogen evolution mechanism of the WS<sub>2</sub>/GCN heterojunction.

Received 5th December 2019

Accepted 28th January 2020

DOI: 10.1039/c9ra10213b

rsc.li/rsc-advances

## 1. Introduction

Semiconductor photocatalytic materials can absorb solar energy for photocatalytic water splitting. This green technology is considered a promising solution for the current problems of environmental pollution and the energy crisis. TiO<sub>2</sub> is the earliest material used for the photocatalytic water splitting into H<sub>2</sub> and O<sub>2</sub>.<sup>1</sup> However, TiO<sub>2</sub> has a wide bandgap (3.2 eV), which indicates that it can only absorb ultraviolet light, and its solar light spectrum utilization rate is only approximately 4%. Searching for a new visible-light photocatalyst has subsequently become a popular topic in the field of solar energy. In recent years, with the discovery of graphene, a large number of two-dimensional semiconductor materials have been used for photocatalytic reactions. These materials have excellent physical properties. For example, graphitic carbon nitride (GCN) not only has a large specific surface area, but it also has a suitable conduction band potential and valence band potential.<sup>2</sup> Transition metal disulfide, such as tungsten disulfide (WS<sub>2</sub>), has a narrow bandgap (approximately 1.8 to 2.1 eV) and high carrier mobility.<sup>3,4</sup> These outstanding advantages enable the material to enhance its photocatalytic performance.<sup>5–7</sup> However, a single

two-dimensional semiconductor material cannot effectively overcome the recombination of photogenerated electrons and holes, and the resultant photocatalytic efficiency is relatively low.<sup>8</sup> At present, an effective solution is to design a heterojunction to reduce the recombination rate of photogenerated carriers and improve the quantum efficiency of photocatalysts.<sup>9,10</sup> A number of studies have reported that photocatalytic properties can be remarkably improved by constructing semiconductor heterostructures, such as phosphorene/g-C<sub>3</sub>N<sub>4</sub>,<sup>11</sup> α-Fe<sub>2</sub>O<sub>3</sub>/g-C<sub>3</sub>N<sub>4</sub>,<sup>12</sup> graphdiyne/g-C<sub>3</sub>N<sub>4</sub>,<sup>13</sup> WO<sub>3</sub>/g-C<sub>3</sub>N<sub>4</sub>,<sup>14</sup> MoS<sub>2</sub>/g-C<sub>3</sub>N<sub>4</sub>,<sup>15</sup> g-C<sub>3</sub>N<sub>4</sub>/TiO<sub>2</sub>,<sup>16</sup> ZnIn<sub>2</sub>S<sub>4</sub>/WS<sub>2</sub>,<sup>17</sup> TiO<sub>2</sub>/WS<sub>2</sub>,<sup>18</sup> *etc.* Recently, a semiconductor heterojunction constructed with WS<sub>2</sub> and GCN is found to have excellent photocatalytic properties.<sup>19–25</sup> Akple *et al.* prepared WS<sub>2</sub>/GCN composites and achieved enhanced photocatalytic activity for H<sub>2</sub> production under visible light.<sup>19</sup> Zhou *et al.* prepared an optimal WS<sub>2</sub>/GCN, with the highest photocatalytic hydrogen evolution at 154 μmol h<sup>-1</sup> g<sup>-1</sup>, a value 34 times higher than that of GCN.<sup>20</sup> WS<sub>2</sub>/GCN nano heterostructures are also widely studied through experiments, but their photocatalytic water splitting mechanisms remain to be contentious. Ma *et al.* investigated the electronic structures of triazine-based GCN/WS<sub>2</sub> composites by performing first-principle calculations.<sup>26</sup> However, in their experiment, the WS<sub>2</sub>/GCN nanocomposites appeared to have a heptazine-based GCN structure instead of a triazine-based GCN structure. Heptazine-based GCNs and triazine-based GCNs completely differ from each other in terms of crystalline and electronic structures. Thus far, no theoretical studies have been conducted on the heptazine-based WS<sub>2</sub>/GCN

<sup>a</sup>School of Physics and Electronic Information, Huaibei Normal University, Huaibei, Anhui, 235000, P. R. China. E-mail: jjliu@chnu.edu.cn

<sup>b</sup>Key Laboratory of Green and Precise Synthetic Chemistry and Applications, Ministry of Education, Huaibei, Anhui, 235000, P. R. China

<sup>c</sup>School of Physical Sciences, University of Science and Technology of China, Hefei 230026, P. R. China


heterojunction photocatalytic mechanism. Therefore, the photocatalytic mechanism of the heptazine-based WS<sub>2</sub>/GCN heterojunction needs to be clarified through theoretical research. Building a reasonable heptazine-based WS<sub>2</sub>/GCN heterojunction and investigating its theoretical microscopic electronic structure to reveal the photocatalytic water splitting mechanism are highly desirable.

In this study, we built heptazine-based WS<sub>2</sub>/GCN heterojunction and calculated its energy bands and density of states (DOS) by using the HSE06 hybrid density functional approach. The charge transfer of the WS<sub>2</sub>/GCN heterojunction was analyzed together with its work function and differential charge density. Then, the separation and mobility processes of the photogenerated electrons and the holes were investigated. A type II heterojunction photocatalytic water splitting mechanism was confirmed.

## 2. Computational methods

All calculations were performed with the Vienna *ab initio* simulation package (vasp).<sup>27</sup> Exchange correction energy was described with the generalized gradient approximation (GGA) of the PBE functional method. The DFT-D3 method with Grimme correction was employed to describe the effect of the vdW interactions.<sup>28</sup> The projector augmented wave method was adopted for the ion–electron forces. The energy cutoff was set to 520 eV, and the Monkhorst–Pack *k*-point mesh was set to  $5 \times 5 \times 1$ . The structural optimizations converged when the energy and the forces reached  $1.0 \times 10^{-5}$  eV and  $0.02 \text{ eV } \text{\AA}^{-1}$  on each atom, respectively. The screened hybrid HSE06 functional method was used to obtain the accurate energy band structures.

## 3. Results and discussion

The 2D/2D WS<sub>2</sub>/GCN nano heterojunction is constructed using a monolayer GCN and a monolayer WS<sub>2</sub>. The heptazine-structured GCN is orthorhombic and belongs to the *Cmc2*<sub>1</sub> space group. The lattice constant ( $a = b = 7.14 \text{ \AA}$ ) of the optimized monolayer GCN is extremely close to the experimental value.<sup>2,29</sup> WS<sub>2</sub> is the trigonal crystal and belongs to the *P3m1* space group. The lattice constant ( $a = b = 3.18 \text{ \AA}$ ) of the optimized monolayer WS<sub>2</sub> only has a 0.95% error relative to the experimental value ( $3.15 \text{ \AA}$ ).<sup>30</sup> The monolayer g-C<sub>3</sub>N<sub>4</sub> nanosheet of the  $\sqrt{3} \times \sqrt{3}$  supercell is placed on the monolayer WS<sub>2</sub> nanosheet of the  $4 \times 4$  supercell as a means to build the WS<sub>2</sub>/GCN heterojunction (Fig. 1a–c). The lattice mismatch ratio between the optimized g-C<sub>3</sub>N<sub>4</sub> supercell and the WS<sub>2</sub> supercell is only 2.9%. The WS<sub>2</sub>/GCN heterojunction contains a total of 90 atoms, including 16 tungsten atoms, 32 sulfur atoms, 18 carbon atoms, and 24 hydrogen atoms. By calculating the minimum value of the energy of the single-layer GCN supercell and the single-layer WS<sub>2</sub> supercell, the optimized lattice constant ( $12.54 \text{ \AA}$ ) can be obtained. This value corresponds to the lattice constant of the 2D/2D WS<sub>2</sub>/GCN heterojunction. The vacuum layer thickness of the WS<sub>2</sub>/GCN heterojunction is set to  $20 \text{ \AA}$  to eliminate the periodic influence of the contiguous layers. The

calculated minimum distance between the two interfaces of the WS<sub>2</sub>/GCN heterojunction is  $3.12 \text{ \AA}$ . The calculated distance between the two interfaces of the WS<sub>2</sub>/GCN heterojunction is extremely close to those of the other calculated GCN-based heterostructures.<sup>31–33</sup>

The C–N covalent bond lengths at the WS<sub>2</sub>/GCN heterojunction are approximately 1.35, 1.36, 1.41, and  $1.50 \text{ \AA}$ , while the W–S covalent bond lengths are 2.40 and  $2.41 \text{ \AA}$ . They hardly differ from the C–N covalent bond lengths (1.33, 1.39, and  $1.48 \text{ \AA}$ ) in the single-layer GCN nano-sheet and from the W–S covalent bond lengths ( $2.41 \text{ \AA}$ ) in the single-layer WS<sub>2</sub> nano-sheet. Therefore, the interaction is very weak between the GCN nano-sheet and the WS<sub>2</sub> nano-sheet.

Interface formation energy is usually used to quantitatively describe the thermodynamic stability of formed heterostructures. The formulaic expression of the formation energy of the interface between GCN and WS<sub>2</sub> is as follows:

$$E_F = E_{\text{WS}_2/\text{GCN}} - E_{\text{WS}_2} - E_{\text{GCN}} \quad (1)$$

where  $E_{\text{WS}_2/\text{GCN}}$ ,  $E_{\text{WS}_2}$ , and  $E_{\text{GCN}}$  represent the total energies of the WS<sub>2</sub>/GCN heterostructure, the single-layer GCN, and the single-layer WS<sub>2</sub> nanosheet, respectively. The formation energy of the WS<sub>2</sub>/GCN heterojunction is  $-2.15 \text{ eV}$ , indicating that the formation of the WS<sub>2</sub>/GCN heterojunction is an exothermic process. The WS<sub>2</sub>/GCN heterojunction has a stable structure in thermodynamics. The calculated interfacial formation energy per unit area is  $15.8 \text{ meV } \text{\AA}^{-2}$ , and the value is within the interface forming energy range generated by the van der Waals interaction.<sup>34</sup> In addition, the distance at the two interfaces of the WS<sub>2</sub>/GCN heterojunction is as high as  $3.12 \text{ \AA}$ . In summary, the WS<sub>2</sub>/GCN heterojunction is a typical van der Waals heterostructure.

We first calculate the energy band structures of the single-layer GCN and the single-layer WS<sub>2</sub> to further investigate the WS<sub>2</sub>/GCN heterojunction (Fig. 2a and b). The single-layer GCN is an indirect bandgap semiconductor with a valence band maximum (VBM) at the  $\Gamma$  high symmetry point and a conduction band minimum (CBM) at the M high symmetry point. The calculated indirect bandgap is  $2.76 \text{ eV}$  based on the HSE06 hybrid functional theory. The calculated result of the HSE06 hybrid functional theory is closer to the experimental value ( $2.7 \text{ eV}$ ) compared with that of the PBE functional method at  $1.36 \text{ eV}$ . The calculated monolayer WS<sub>2</sub> is a direct bandgap semiconductor, and the CBM and the VBM are both located at the high symmetry point of K. The direct bandgap of the monolayer WS<sub>2</sub> calculated by HSE06 hybrid functional approach is  $2.28 \text{ eV}$ , while the result calculated by the PBE functional approach is  $1.59 \text{ eV}$ . The bandgap of the monolayer WS<sub>2</sub> measured experimentally is approximately  $2.0 \text{ eV}$ .<sup>35</sup> The comparison indicates that the monolayer WS<sub>2</sub> bandgap calculated by the HSE06 hybrid functional approach is closer to the experimental value and more precise than that calculated by the PBE functional.

The project energy band structure of the WS<sub>2</sub>/GCN heterojunction is calculated by the HSE06 hybrid functional approach (Fig. 3). The WS<sub>2</sub>/GCN heterojunction is a typical indirect bandgap semiconductor structure and its bandgap is  $2.34 \text{ eV}$



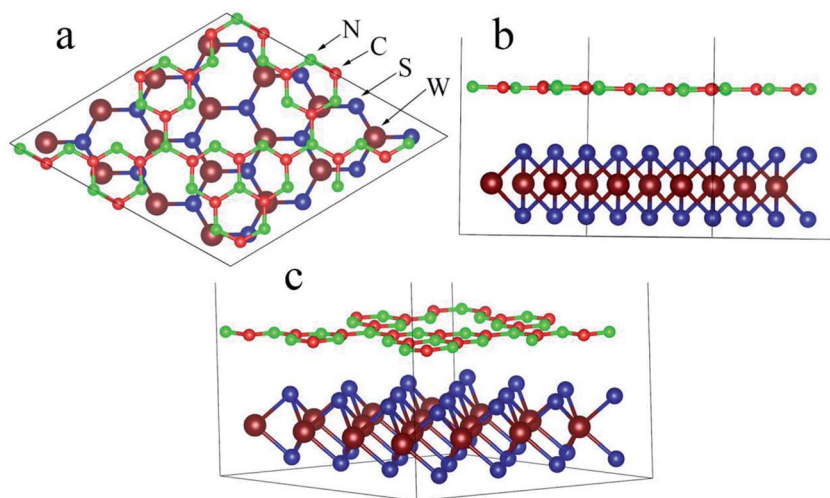


Fig. 1 (a) Vertical view, (b) lateral view, and (c) three dimensional optimal  $\text{WS}_2/\text{GCN}$  heterojunction.

(Fig. 3a). The CBM of the heterojunction is located at the  $\Gamma$  point, by contrast, the VBM is not located at the high-symmetry point, and instead positioned between the high-symmetry points of M and K. Different from the energy band structures of the monolayer GCN and the monolayer  $\text{WS}_2$ , the energy band structure of the  $\text{WS}_2/\text{GCN}$  heterojunction is not just a simple addition of the energy band structures of GCN and  $\text{WS}_2$ . The CBM and the VBM of the  $\text{WS}_2/\text{GCN}$  heterojunction have both changed. At this point, the van der Waals interactions between the monolayer GCN and the  $\text{WS}_2$  nanosheet are affected by the energy band structure of the  $\text{WS}_2/\text{GCN}$  heterojunction. In the conduction band region, the lowest energy orbitals of the conduction band belong to GCN, whereas the relatively high energy orbitals of the conduction band belong to  $\text{WS}_2$ . The CBM

of the  $\text{WS}_2/\text{GCN}$  heterojunction is composed of the electron orbitals of GCN (Fig. 3b). In the valence band region, the highest energy orbitals of the conduction band are occupied by  $\text{WS}_2$ , whereas the relatively low energy levels of the valence band are occupied by GCN. The VBM of the  $\text{WS}_2/\text{GCN}$  heterojunction is composed of the electron orbitals of  $\text{WS}_2$  (Fig. 3c). The band edges of GCN and  $\text{WS}_2$  are shaped similar to a ladder, and the  $\text{WS}_2/\text{GCN}$  heterojunction has a type II structure.

We calculated the total density of states (TDOS) and the partial density of states (PDOS) of  $\text{WS}_2/\text{GCN}$  heterojunction by using HSE06 hybrid functional approach to further study the composition of the microelectronic structure. The VBM of the  $\text{WS}_2/\text{GCN}$  heterojunction is mainly composed of W 5d and S 3p orbits, and also contains a small number of W 6s and W 5p

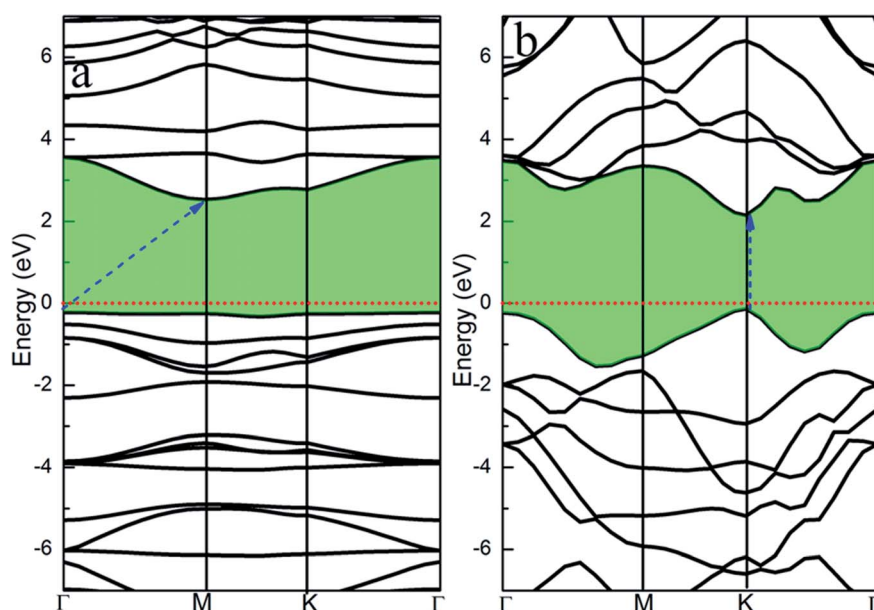


Fig. 2 Energy band structures of monolayer (a) GCN and (b)  $\text{WS}_2$  nanosheet.





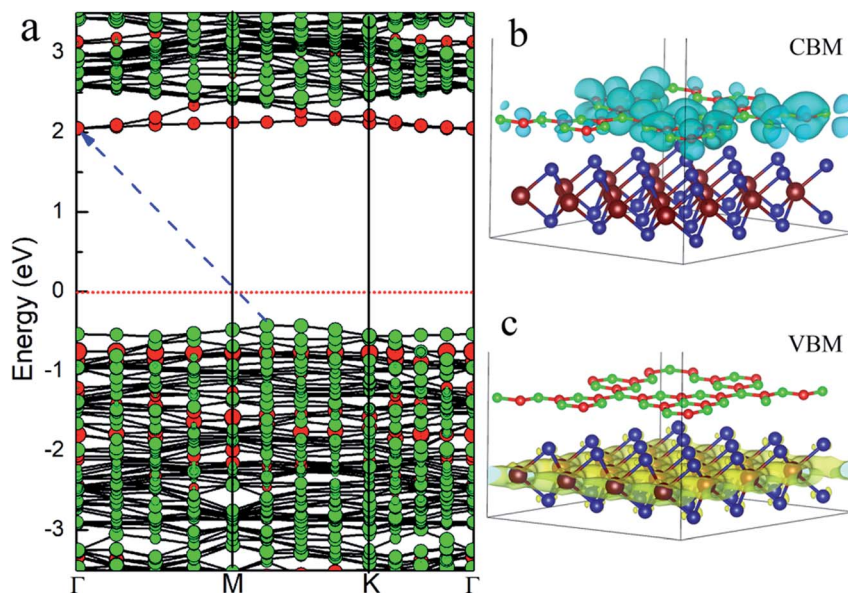


Fig. 3 (a) The project energy band structure of WS<sub>2</sub>/GCN heterojunction; (b) the electron orbitals in the CBM and (c) VBM of WS<sub>2</sub>/GCN heterojunction.

orbits. The ratios were 77%, 19.5%, 1.7% and 1.5%, respectively. While the CBM of the WS<sub>2</sub>/GCN heterojunction is mainly occupied by C 2p and N 2p orbits, and also includes a small number of N 2s orbits. The ratios were 65.3%, 34.1% and 0.5%, respectively (Fig. 4). The configuration differs from the orbital composition of the monolayer GCN and the WS<sub>2</sub> nanosheet. The van der Waals force between the GCN nanosheet and the WS<sub>2</sub> nanosheet has changed the distribution of the electrons in

the WS<sub>2</sub>/GCN heterojunction, and it has a type II heterostructure, which is consistent with the previous band structure's analytical results. The WS<sub>2</sub>/GCN heterojunction, as a type II structure, is conducive in promoting the separation of photo-excited electrons and holes, subsequently improving photocatalytic activity effectively.

The interaction between the interfaces of the heterostructure will change the charge distribution on the two surfaces. Therefore, a built-in electric field will be formed within the heterostructure. This phenomenon can affect the transfer of photogenerated electrons and holes and further affect the photocatalytic performance of the heterojunction. Thus, an analysis of the charge distribution between the interfaces of the WS<sub>2</sub>/GCN heterojunction is extremely important.

First, we investigated the differential charge density distribution of the WS<sub>2</sub>/GCN heterojunction. The formula of the differential charge density is as follows:

$$\Delta\rho = \rho_{\text{WS}_2/\text{GCN}} - \rho_{\text{GCN}} - \rho_{\text{WS}_2} \quad (2)$$

where  $\rho_{\text{WS}_2/\text{GCN}}$ ,  $\rho_{\text{GCN}}$ , and  $\rho_{\text{WS}_2}$  are the charge densities of the WS<sub>2</sub>/GCN heterojunction, the single-layer GCN, and the WS<sub>2</sub> nanosheet, respectively. The calculated differential charge density distributions of the WS<sub>2</sub>/GCN heterojunction are shown in the Fig. 5a and b. In these figures, cyan represents electron loss, while yellow represents electron accumulation. The charge density distribution on the GCN interface is mainly cyan and accompanied by a small amount of yellow. The color plots indicate that electrons are lost at the GCN interface and aggregate holes, and the GCN interface is positively charged. On the contrary, the charge density distribution on the WS<sub>2</sub> interface is mainly yellow and accompanied with some cyan. The color plots indicate that electrons are accumulated at the WS<sub>2</sub> interface, and the WS<sub>2</sub> interface is negatively charged. We

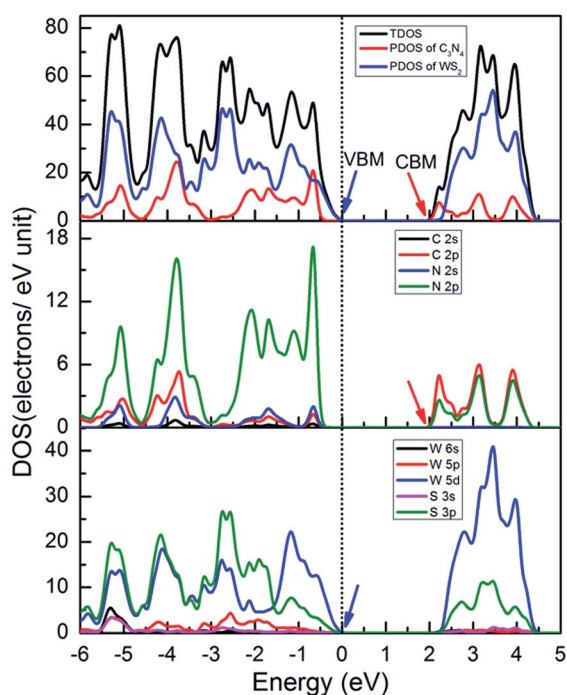


Fig. 4 The TDOS and PDOS of WS<sub>2</sub>/GCN heterojunction.



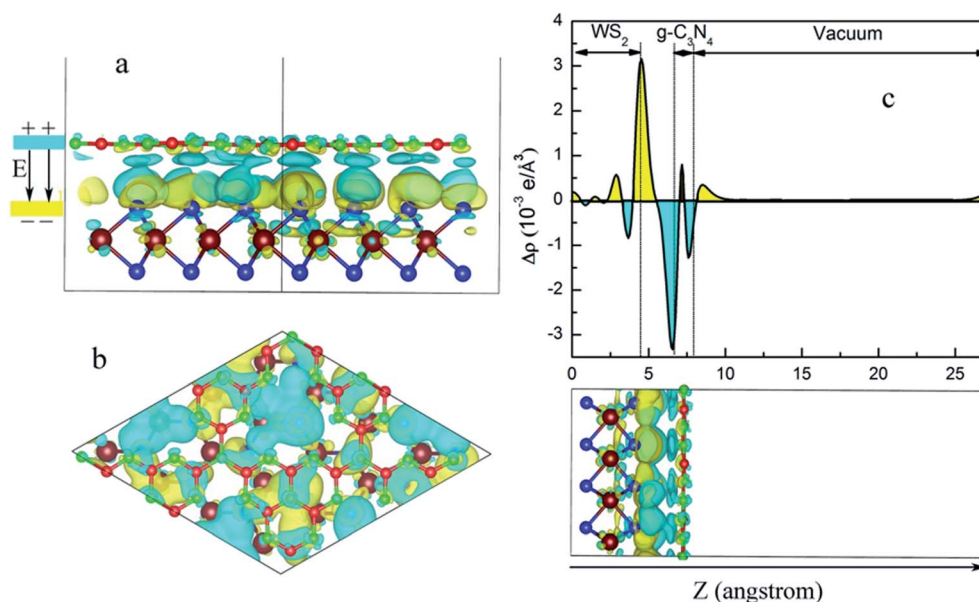


Fig. 5 (a) The lateral view and (b) vertical view of the charge density difference of WS<sub>2</sub>/GCN heterojunction. (c) Electron density difference of plane projection along with Z axis for the WS<sub>2</sub>/GCN heterojunction.

further project the differential charge density to the Z axis (Fig. 5c). The figure intuitively implies that the GCN interface is positively charged, and the WS<sub>2</sub> interface is negatively charged. A built-in electric field exists, and its direction is from the GCN interface to the WS<sub>2</sub> interface within the WS<sub>2</sub>/GCN heterojunction.

Second, we calculate the work functions of the monolayer WS<sub>2</sub>, the GCN nanosheet, and the WS<sub>2</sub>/GCN heterojunction to investigate the charge transfers between the WS<sub>2</sub>/GCN interface. The work function represents the minimum energy needed to lift an electron from the Fermi level to the vacuum. The formula of the work function is as follows:

$$\Phi = E_{\text{vac}} - E_{\text{Fermi}} \quad (3)$$

where  $\Phi$ ,  $E_{\text{vac}}$ , and  $E_{\text{Fermi}}$  are the work function, the vacuum energy level, and the Fermi energy level, respectively.<sup>33</sup> The calculated work functions of the single-layer WS<sub>2</sub>, the GCN nanosheet, and the WS<sub>2</sub>/GCN heterojunction are 5.97, 5.81, and 5.86 eV, respectively (Fig. 6a–c). As the GCN nanosheet and the WS<sub>2</sub> nanosheet come into contact, the electrons on the GCN nanosheet flow into the WS<sub>2</sub> nanosheet owing to the Fermi energy level of the former is higher than that of the latter. The charge distribution at the interface will reach a thermal equilibrium when their Fermi energy levels become equal. Then, as parts of the electrons transfer from the GCN nanosheet to the WS<sub>2</sub> nanosheet, the former becomes positively charged, whereas the latter becomes negatively charged. Therefore, a stable built-in electric field ( $V_D$ ) is formed between the WS<sub>2</sub>/GCN heterojunction interfaces. The value of  $V_D$  is 0.16 V, and its direction is from the GCN nanosheet to the WS<sub>2</sub> nanosheet. The result of the work function analysis is consistent with that of the differential charge density distribution analysis.

The VBM and CBM potentials of a semiconductor are the main factors of photocatalytic redox capacity. A positive VBM potential means strong oxidation capacity, while a negative CBM potential means strong reduction ability. Combined with the calculation for energy band structure, DOS, and electrostatic potential, we can further study the mechanism of the photocatalytic water splitting in the WS<sub>2</sub>/GCN heterojunction. According to the work function calculation, WS<sub>2</sub> and GCN differ in their Fermi energy levels. When WS<sub>2</sub> and GCN form a WS<sub>2</sub>/GCN heterojunction, the energy bands of the WS<sub>2</sub> and the GCN will bend. The energy band of WS<sub>2</sub> has a downward bending amount ( $qV_{D2}$ ) of 0.11 eV, the energy band of GCN has an upward bending amount ( $qV_{D1}$ ) of 0.06 eV, and the total band bending amount ( $qV_D$ ) is 0.16 eV, where  $V_D$  is the potential of the built-in electric field between two interfaces of the WS<sub>2</sub>/GCN heterojunction. From the calculated results of the electrostatic potential and the DOS of the WS<sub>2</sub>/GCN heterojunction, we can derive the CBM and VBM potentials of the WS<sub>2</sub>/GCN heterojunction. The details are shown in Fig. 7. The CBM and VBM potentials of WS<sub>2</sub> are −0.87 and 1.66 V (vs. NHE), respectively. Meanwhile, the CBM and VBM potentials of GCN are −0.67 V and 2.09 V, respectively. The conduction band offset ( $\Delta E_C$ ) and the valence band offset ( $\Delta E_V$ ) of the WS<sub>2</sub>/GCN heterojunction are 0.04 and 0.27 eV, respectively. When irradiated with light, the electrons on the valence bands of WS<sub>2</sub> and GCN are excited to the conduction band. Meanwhile, the same number of holes are generated on the valence bands of WS<sub>2</sub> and GCN. Driven by built-in electric field forces, the electrons on the conduction bands of WS<sub>2</sub> transfer to the conduction bands of GCN, while the holes on the valence bands of GCN transfer to the valence bands of WS<sub>2</sub>. Consequently, the photoexcited electrons and holes gather in the conduction bands of GCN and the valence bands of WS<sub>2</sub>, respectively. These phenomena result in the



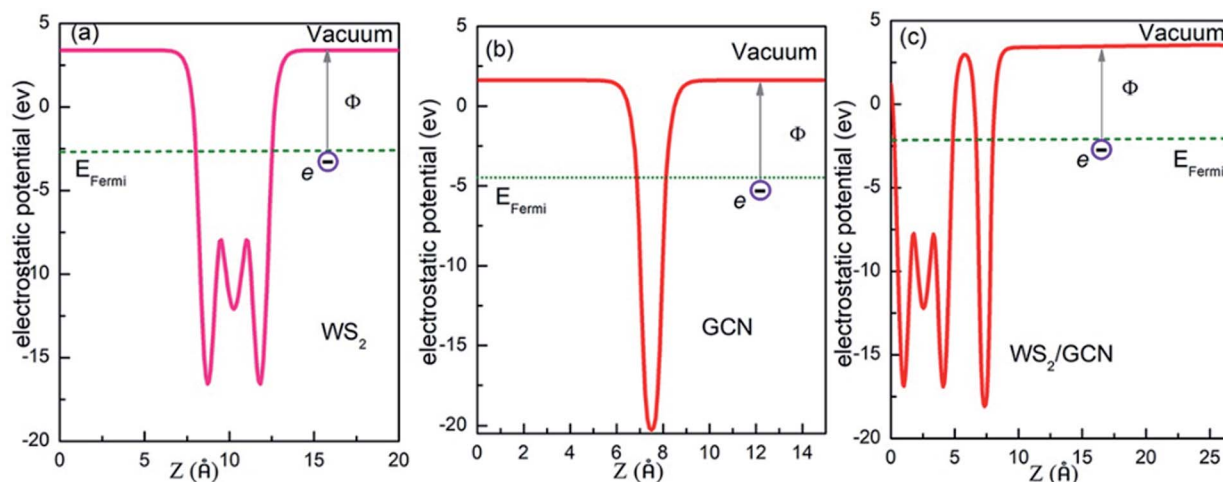


Fig. 6 The electrostatic potential of (a) monolayer  $\text{WS}_2$ , (b) GCN nanosheets and (c)  $\text{WS}_2/\text{GCN}$  heterojunction.

separation of photoexcited electrons and holes in space, effectively avoiding a large number of recombination of photoexcited electrons and holes, and they extend the lifetime of the

photoexcited carriers. Therefore, the photogenerated electrons and the holes can further increase the probability of surface photocatalytic reaction, effectively improving the photocatalytic

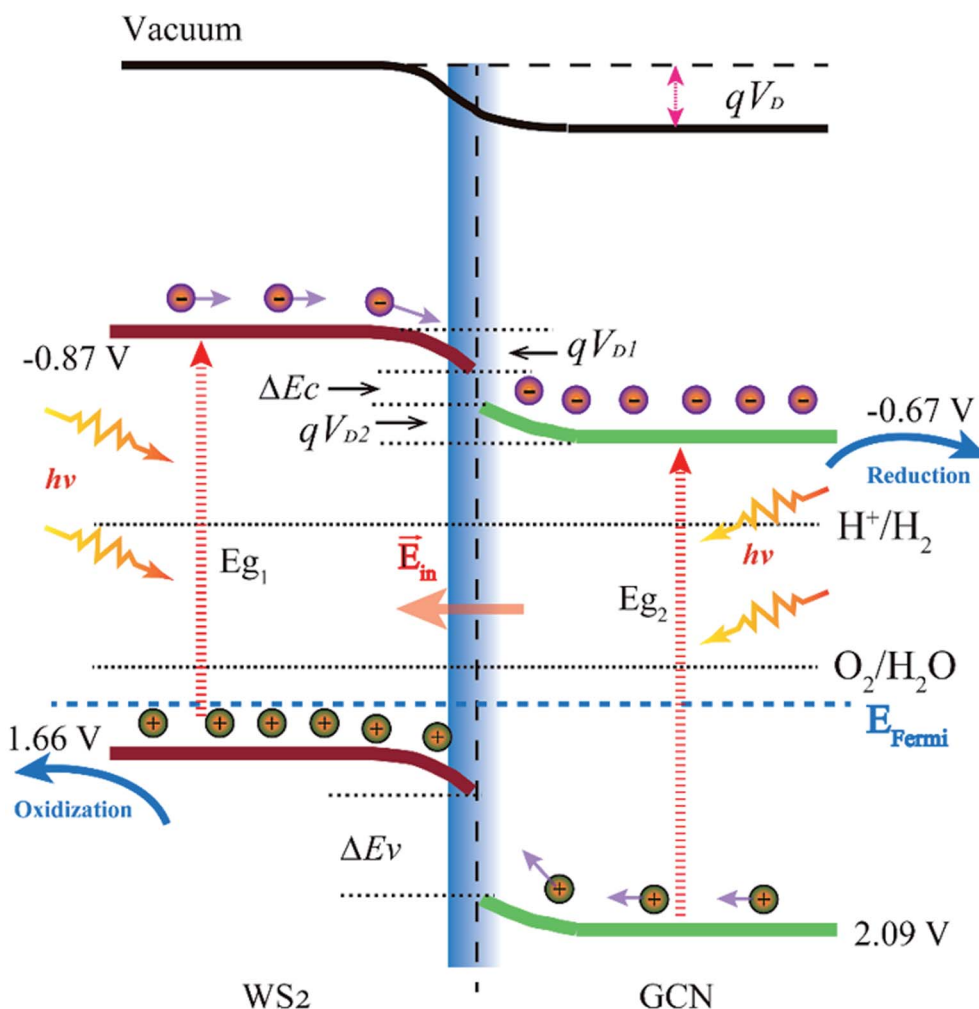


Fig. 7 Photocatalytic mechanism of type II  $\text{WS}_2/\text{GCN}$  heterojunction.



efficiency of the WS<sub>2</sub>/GCN heterojunction. The photoexcited electrons' potential in the CBM of GCN is  $-0.67$  V, which is negative relative to the reduction potential of H<sup>+</sup>/H<sub>2</sub> (0 V), indicating sufficient ability to reduce hydrogen ion to hydrogen. Meanwhile, the photogenerated holes' potential in the VBM of WS<sub>2</sub> is  $1.66$  V, which is more positive than the potential of O<sub>2</sub>/H<sub>2</sub>O ( $1.23$  V), suggesting sufficient ability to oxidize water to oxygen. The results of the theoretical analysis are consistent with the experimental study. In summary, the WS<sub>2</sub>/GCN heterojunction has a type II photocatalytic structure with staggered energy levels. This configuration can effectively promote the separation of photogenerated electrons and holes in space, and it has enough potential to decompose water to produce hydrogen and oxygen.

## 4. Conclusion

In this work, the electronic structures and the photocatalytic water decomposition of the WS<sub>2</sub>/GCN heterojunction are systematically investigated by using the hybrid density functional approach. The bandgap of the monolayered WS<sub>2</sub>, the GCN nanosheet and the WS<sub>2</sub>/GCN heterojunction are  $2.28$ ,  $2.76$ , and  $2.34$  eV, respectively. The calculated interfacial formation energy and the interface distance indicate that the interface interaction of the WS<sub>2</sub>/GCN heterojunction belong to a van der Waals force. Furthermore, the WS<sub>2</sub>/GCN heterojunction has a typical van der Waals heterostructure. The energy band structures and the DOS calculations reveal that the WS<sub>2</sub>/GCN heterojunction has a typical type-II heterostructure, and its valence band offset and conduction band offset are  $0.27$  and  $0.04$  eV, respectively. The different Fermi energy levels of the monolayer WS<sub>2</sub> and the GCN nanosheet causes the energy band to bend at the interface when they form a heterojunction. The total band bending amount ( $qV_D$ ) is  $0.16$  eV, and the potential of the built-in electric field between the interfaces of the WS<sub>2</sub>/GCN heterojunction is  $0.16$  V. The built-in electric field can promote the separation of the photoexcited electrons and the holes in space, and a large number of recombination of photoexcited electrons and holes can be effectively avoided. Therefore, photogenerated electrons and holes can further increase the probability of surface photocatalytic reaction, effectively improving the photocatalytic efficiency of the WS<sub>2</sub>/GCN heterojunction. In terms of WS<sub>2</sub>/GCN heterojunction photocatalytic water decomposition, the photoexcited electrons' potential in the CBM of GCN is  $-0.67$  V, which is negative relative to the reduction potential of H<sup>+</sup>/H<sub>2</sub> (0 V), indicating sufficient ability to reduce hydrogen ion to hydrogen. Meanwhile, the photogenerated holes' potential in the VBM of WS<sub>2</sub> is  $1.66$  V, which is more positive than the potential of O<sub>2</sub>/H<sub>2</sub>O ( $1.23$  V), suggesting sufficient the ability to oxidize water to oxygen. Our work not only elucidates the photocatalytic water decomposition mechanism of the WS<sub>2</sub>/GCN heterostructure but also provides a good idea for designing photocatalytic heterojunctions.

## Conflicts of interest

There are no conflicts to declare.

## Acknowledgements

This work was supported by Anhui Provincial Natural Science Foundation (No. 1908085MA23 and 1908085QE222) and Natural Science Foundation of Education Department of Anhui Province (No. KJ2017A385)

## Notes and references

- 1 A. Fujishima and K. Honda, *Nature*, 1972, **238**, 37–38.
- 2 X. Wang, K. Maeda, A. Thomas, K. Takanabe, G. Xin, J. M. Carlsson, K. Domen and M. Antonietti, *Nat. Mater.*, 2009, **8**, 76–80.
- 3 Y. Sang, Z. Zhao, M. Zhao, P. Hao, Y. Leng and H. Liu, *Adv. Mater.*, 2015, **27**, 363–369.
- 4 V. Q. Bui, T. T. Pham, D. A. Le, C. M. Thi and H. M. Le, *J. Phys.: Condens. Matter*, 2015, **27**, 305005.
- 5 B. Mahler, V. Hoepfner, K. Liao and G. A. Ozin, *J. Am. Chem. Soc.*, 2014, **136**, 14121–14127.
- 6 C. Tan, X. Cao, X. J. Wu, Q. He, J. Yang, X. Zhang, J. Chen, W. Zhao, S. Han, G. H. Nam, M. Sindoro and H. Zhang, *Chem. Rev.*, 2017, **117**, 6225–6331.
- 7 H. Huang, K. Xiao, N. Tian, F. Dong, T. Zhang, X. Du and Y. Zhang, *J. Mater. Chem. A*, 2017, **5**, 17452–17463.
- 8 M. Yousefi, M. Faraji, R. Asgari and A. Z. Moshfegh, *Phys. Rev. B*, 2018, **97**, 195428.
- 9 T. Su, Q. Shao, Z. Qin, Z. Guo and Z. Wu, *ACS Catal.*, 2018, **8**, 2253–2276.
- 10 N. Tian, H. Huang, X. Du, F. Dong and Y. Zhang, *J. Mater. Chem. A*, 2019, **7**, 11584–11612.
- 11 J. R. Ran, W. W. Guo, H. L. Wang, B. C. Zhu, J. G. Yu and S. Z. Qiao, *Adv. Mater.*, 2018, **30**, 6.
- 12 X. J. She, J. J. Wu, H. Xu, J. Zhong, Y. Wang, Y. H. Song, K. Q. Nie, Y. Liu, Y. C. Yang, M. T. F. Rodrigues, R. Vajtai, J. Lou, D. L. Du, H. M. Li and P. M. Ajayan, *Adv. Energy Mater.*, 2017, **7**, 7.
- 13 Q. L. Xu, B. C. Zhu, B. Cheng, J. G. Yu, M. H. Zhou and W. K. Ho, *Appl. Catal., B*, 2019, **255**, 10.
- 14 J. W. Fu, Q. L. Xu, J. X. Low, C. J. Jiang and J. G. Yu, *Appl. Catal., B*, 2019, **243**, 556–565.
- 15 Y. J. Yuan, Z. K. Shen, S. T. Wu, Y. B. Su, L. Pei, Z. G. Ji, M. Y. Ding, W. F. Bai, Y. F. Chen, Z. T. Yu and Z. G. Zou, *Appl. Catal., B*, 2019, **246**, 120–128.
- 16 J. G. Yu, S. H. Wang, J. X. Low and W. Xiao, *Phys. Chem. Chem. Phys.*, 2013, **15**, 16883–16890.
- 17 W. Pudkon, S. Kaowphong, S. Pattison, P. J. Miedziak, H. Bahruji, T. E. Davies, D. J. Morgan and G. J. Hutchings, *Catal. Sci. Technol.*, 2019, **9**, 5698–5711.
- 18 Y. C. Wu, Z. M. Liu, Y. R. Li, J. T. Chen, X. X. Zhu and P. Na, *Chin. J. Catal.*, 2019, **40**, 60–69.
- 19 M. S. Akple, J. X. Low, S. Wageh, A. A. Al-Ghamdi, J. G. Yu and J. Zhang, *Appl. Surf. Sci.*, 2015, **358**, 196–203.
- 20 Y. L. Zhou, X. Y. Ye and D. Y. Lin, *Int. J. Hydrogen Energy*, 2019, **44**, 14927–14937.
- 21 M. M. Shao, W. Z. Chen, S. J. Ding, K. H. Lo, X. W. Zhong, L. M. Yao, W. F. Ip, B. M. Xu, X. S. Wang and H. Pan, *ChemSusChem*, 2019, **12**, 3355–3362.



- 22 P. Zeng, X. Y. Ji, Z. G. Su and S. P. Zhang, *RSC Adv.*, 2018, **8**, 20557–20567.
- 23 Y. N. Ma, J. Li, E. Z. Liu, J. Wan, X. Y. Hu and J. Fan, *Appl. Catal., B*, 2017, **219**, 467–478.
- 24 H. H. Tran, D. H. Truong, T. T. Truong, T. Xuan Dieu Nguyen, Y.-S. Jin, S. J. Kim and V. Vo, *Bull. Korean Chem. Soc.*, 2018, **39**, 965–971.
- 25 J. Huang, J. Mei, J. Han, H. Liang, W. Wang, B. Dong and L. Cao, *J. Colloid Interface Sci.*, 2019, **556**, 224–231.
- 26 X. G. Ma, C. Chen, J. S. Hu, M. K. Zheng, H. H. Wang, S. J. Dong, C. Y. Huang and X. B. Chen, *J. Alloys Compd.*, 2019, **788**, 1–9.
- 27 G. Kresse and J. Furthmüller, *Phys. Rev. B: Condens. Matter Mater. Phys.*, 1996, **54**, 11169–11186.
- 28 S. Grimme, *J. Comput. Chem.*, 2006, **27**, 1787–1799.
- 29 J. Gracia and P. Kroll, *J. Mater. Chem.*, 2009, **19**, 3013–3019.
- 30 W. J. Schutte, J. L. De Boer and F. Jellinek, *J. Solid State Chem.*, 1987, **70**, 207–209.
- 31 J. Wang, Z. Guan, J. Huang, Q. Li and J. Yang, *J. Mater. Chem. A*, 2014, **2**, 7960–7966.
- 32 J. Zhang, F. Ren, M. Deng and Y. Wang, *Phys. Chem. Chem. Phys.*, 2015, **17**, 10218–10226.
- 33 J. Liu, *J. Phys. Chem. C*, 2015, **119**, 28417–28423.
- 34 T. Björkman, A. Gulans, A. V. Krasheninnikov and R. M. Nieminen, *Phys. Rev. Lett.*, 2012, **108**, 235502.
- 35 Y. Sun, H. Cheng, S. Gao, Z. Sun, Q. Liu, Q. Liu, F. Lei, T. Yao, J. He, S. Wei and Y. Xie, *Angew. Chem., Int. Ed.*, 2012, **51**, 8727–8731.

